The HD 206893 planetary system seen with VLT/SPHERE: upper limit on the dust albedo and constraints on additional companions

Romero, C.; Milli, J.; Lagrange, A.-M.; Holstein, R.G. van; Cantalloube, F.; Marino, S.; Ray, S.

Citation

Astronomy
&
Astrophysics

The HD 206893 planetary system seen with VLT/SPHERE

Upper limit on the dust albedo and constraints on additional companions

C. Romero[1,2], J. Milli[1,2], A.-M. Lagrange[1], R. G. van Holstein[2,3], F. Cantalloube[4], S. Marino[5,6], and S. Ray[7]

[1] Univ. Grenoble Alpes, CNRS, IPAG, 38000 Grenoble, France
[2] European Southern Observatory, Alonso de Córdova 3107, Vitacura, Casilla 19001, Santiago de Chile, Chile
  e-mail: cromero@eso.org
[3] Leiden Observatory, Leiden University, PO Box 9513, 2300 RA Leiden, The Netherlands
[4] Max Planck Institute for Astronomy, Königstuhl 17, 69117 Heidelberg, Germany
[5] Institute of Astronomy, University of Cambridge, Madingley Road, Cambridge CB3 0HA, UK
[6] Jesus College, University of Cambridge, Jesus Lane, Cambridge CB5 8BL, UK
[7] Astrophysics Group, University of Exeter, Physics Building, Stocker Road, Devon EX4 4QL, UK

ABSTRACT

Context. The detection and characterization of planets and debris disks is a very active field in current research. The F5V star HD 206893 hosts a $\sim$25 $M_{\rm Jup}$ brown dwarf detected at $\sim$10 au in VLT/SPHERE high-contrast images. This system is also known to host a debris disk, which is inferred from its high infrared excess. This disk was recently resolved in thermal submillimeter imaging with ALMA and extends from 30 to 180 au, with a $\sim$27 au wide gap at $\sim$74 au.
Aims. Our goal is to search for the scattered light emission of the disk using the largest amount of SPHERE imaging data available to date. We also want to bring tighter constraints on the presence of additional low-mass companions based on the available multi-epoch high-contrast imaging data.
Methods. We analyzed six epochs of SPHERE near-infrared data, processed with angular, polarimetric, and reference differential imaging, in order to detect the disk around HD 206893.
Results. We do not detect the debris disk. Based on recent constraints on the disk morphology from ALMA data, this non-detection is compatible with a maximum albedo of 0.55 in the H band and 0.96 in the K band. Furthermore, we do not detect additional low-mass companions in the system. A low-mass companion is expected from radial velocity and astrometric measurements between 1.4 and 2.6 au, and we estimate our probability of detection higher than 90% for brown dwarfs more massive than 55 $M_{\rm Jup}$ in this separation range. At 74 au, where a gap is detected in the disk in thermal imaging, this probability of detection corresponds to planets above 2.5 $M_{\rm Jup}$.
Conclusions. The non-detection of the disk through the methods used in this study should not exclude an attempt with other techniques, such as advanced reference-star differential imaging using machine-learning-based libraries or star hopping. Furthermore, the future JWST instrument NIRCam might offer the possibility of detecting the disk in scattered light thanks to its increased sensitivity.

Key words. planet-disk interactions – instrumentation: high angular resolution – techniques: image processing – planetary systems

1. Introduction

Debris disks around stars have generally been detected by their excess emission at infrared wavelengths (Hughes et al. 2018). Resolving those debris disks in scattered light through high-contrast imaging is challenging because they are usually faint and close to their parent star. In addition, it is particularly difficult to disentangle this faint and extended signal from the bright starlight residuals for disks that show circular symmetry (e.g., seen pole-on or with a small inclination with respect to the line of sight). Nevertheless, since the first images in the 1990s, dozens of such disks have been resolved, both from space and from the ground (e.g., Esposito et al. 2020; Hughes et al. 2018; Schneider et al. 2016).

A circumstellar debris disk was inferred around HD 206893 through its large infrared excess ($L_{\rm dust}/L_\star = 2.3 \times 10^{-4}$, Moór et al. 2006). It was characterized using its spectral energy distribution (SED) with the Infrared Spectrograph (IRS) and the Multiband Imaging Photometer for *Spitzer* (MIPS) on board the *Spitzer* Space Telescope (Chen et al. 2014) and marginally resolved by the Photodetector Array Camera and Spectrometer (PACS) on the *Herschel* Space Observatory (Milli et al. 2017). A tentative detection in scattered light using the VLT/Spectro-Polarimetric High-contrast Exoplanet REsearch instrument (SPHERE) was reported by Milli et al. (2017). HD 206893 is an F5V, 250^{+450}_{-200} Myr old star (Delorme et al. 2017) located at 40.81 ± 0.11 pc (Gaia Collaboration 2018). It has an apparent V magnitude of 6.67 (Høg et al. 2000), a mass of 1.32 ± 0.02 $M_\odot$, and an effective temperature of 6500.0 ± 100 K (Delorme et al. 2017). Recently, Marino et al. (2020) and Nederlander et al. (2021) resolved the disk using ALMA data taken in band 7 at a wavelength of 0.8 mm and archival data from band 6 at a wavelength of 1.3 mm.

Furthermore, the star is known to host a low-mass companion (Milli et al. 2017), HD 206893 B, that is orbiting at a projected separation of $\sim$10 au. Delorme et al. (2017) found a period of $\sim$27 yr and a mass between 12 and 50 $M_{\rm Jup}$, for an age in the range 50–700 Myr. As the age of the system is poorly known, the

Table 1. Observing log.

Night	Program ID	Mode/Filter/Coronagraph	DIT (s) × NDIT × Nexp	t_{total} [a] (h)	AM [b]	$\Delta\theta$ [c] (°)	Seeing [d] (″)	τ_0 [d] (ms)	Wind speed [e] (m s^{-1})	TN [f] (°)	Pls [g] (mas pix^{-1})
2015-10-03	096.C-0388(A)	CI/BB_H/N_ALC_YJH_S	4 × 36 × 16	0.64	1.02	49.2	0.87	3.0	3.5	−1.82	12.25
2016-09-15	097.C-0865(D)	DBI/K1K2/N_ALC_Ks	64 × 5 × 16	1.42	1.03	75.9	0.64	5.0	8.6	−1.76	12.26
2017-07-13	099.C-0708(A)	CI/BB_H/N_ALC_YJH_L	64 × 9 × 17	2.72	1.04	109.0	0.75	4.3	4.0	−1.75	12.25
2018-06-19	1100.C-0481(H)	DBI/K1K2/N_ALC_Ks	64 × 15 × 6	1.60	1.02	76.1	0.51	5.6	5.9	−1.78	12.26
2018-09-05	0101.C-0502(B)	DPI/BB_K/N_ALC_Ks	32 × 1 × 68	0.60	1.03	31.6	0.54	8.5	4.5	−1.75	12.25
2018-09-07	0101.C-0502(B)	DPI/BB_K/N_ALC_Ks	32 × 1 × 76	0.68	1.03	33.7	0.62	14.7	0.8	−1.75	12.25

Notes. [a]Total time spent integrating in coronagraphic imaging. [b]Mean airmass. [c]Amplitude of parallactic angle variation during the coronagraphic sequence. [d]Measured with the MASS-DIMM. [e]Measured at 30 m with the Astronomical Site Monitoring. [f]True north. [g]Plate scale.

estimated mass of HD 206893 B, derived from brightness-mass relations, is still poorly constrained.

By combining and analyzing data from six epochs obtained with SPHERE, the largest amount of data available to date, this study aims at complementing the information obtained by Milli et al. (2017). It intends to verify if the scattered light emission of the debris disk is detected through high-contrast imaging by ruling out some instrumental effects that could lead to a false detection, such as the low-wind effect (LWE; Milli et al. 2018) or the wind-driven halo (Cantalloube et al. 2018, 2020). Based on the results from Marino et al. (2020), we also discuss the surface brightness and dust albedo of the disk.

Grandjean et al. (2019) report variations in the radial velocity (RV) of the star, attributing these variations to an additional companion, HD 206893 C, with an orbital semimajor axis between 1.4 and 2.6 au and a mass of approximately 15 M_{Jup}. This is consistent with the subsequent results by Marino et al. (2020), who found that the inner companion could also be responsible for the proper motion anomaly that this system has. The ALMA images reveal a 27 ± 5 au wide gap in the disk at 74 ± 3 au, which would be compliant with yet another companion, a planet of $0.9^{+0.8}_{-0.5}$ M_{Jup} at a separation of ~1.81″. Combining all but the polarimetric data, we estimate constraints on the presence of other companions in the system in addition to HD 206893 B.

The SPHERE observations and data we use are presented in Sect. 2. Section 3 presents the contrast results in order to determine if there is a signal consistent with the disk. In Sect. 4, we present a discussion on the albedo of the dust. In Sect. 5, we show the probability of planet detection around HD 206893 using this combined data set, and in Sect. 6 we conclude and summarize our results.

2. Observations

The six epochs were obtained with the SPHERE high-contrast instrument (Beuzit et al. 2019) between October 2015 and August 2018, using the InfraRed Dual-band Imager and Spectrograph (IRDIS; Dohlen et al. 2008) in different modes: classical imaging (CI, also referred as broadband imaging), dual-band imaging (DBI; Vigan et al. 2010), and dual-beam polarimetric imaging (DPI; Langlois et al. 2014), as described in Table 1.

2.1. IRDIS broadband and dual-band imaging data

We used archival data obtained in DBI in the *K1-K2* filter as part of the SpHere INfrared survey for Exoplanets (SHINE; Desidera

et al., in prep.; Langlois et al., in prep.; Vigan et al. 2021). These data were presented in Delorme et al. (2017), for the September 15, 2016, observations, and in Grandjean et al. (2019), for the June 19, 2018, observations. We also used archival data obtained in the broadband *K* filter as part of the SPHERE High Angular Resolution Debris Disk Survey (SHARDDS; Wahhaj et al. 2016; Choquet et al. 2018). These data were presented in Milli et al. 2017, for the October 3, 2015, observations, and in Grandjean et al. 2019, for the July 13, 2017, observations. They were reduced using classical Angular Differential Imaging (cADI; Marois et al. 2006) and principal component analysis (PCA; Soummer et al. 2012) by the SPHERE Data Center, as described in Delorme et al. (2017), and using ANDROMEDA (Cantalloube et al. 2015).

2.2. IRDIS DPI data

The DPI observations are presented in van Holstein et al. (in prep.) and briefly described here. They were obtained in the *K* band on September 5 and 7, 2018, using the apodized Lyot coronagraph with a mask of 240 mas diameter (Carbillet et al. 2011; Guerri et al. 2011). They used the pupil-tracking mode to enable angular differential imaging (ADI; Marois et al. 2006) and to take advantage of the fact that in this mode the polarimetric efficiency is always high and the diffraction patterns of the secondary mirror support structure are suppressed (van Holstein et al. 2017). Using a detector integration time (DIT) of 32s, a total of 36 half-wave plate (HWP) cycles was obtained, resulting in a total on-source integration time of 77 min for the two epochs. The conditions were excellent, with an average atmospheric seeing and coherence time of approximately 0.6″ and 12 ms, respectively.

We reduced these data with IRDIS Data reduction for Accurate Polarimetry[1] (IRDAP; van Holstein et al. 2020, 2017), a highly automated pipeline that reduces IRDIS polarimetric data using polarimetric differential imaging (PDI). After conventional preprocessing steps, IRDAP computes Stokes Q and U images using the double difference method. It then corrects the images for instrumental polarization and crosstalk using an experimentally validated Mueller matrix model and computes the final Q and U images. Finally, IRDAP calculates the Q_ϕ and U_ϕ images following the definitions presented in de Boer et al. (2020).
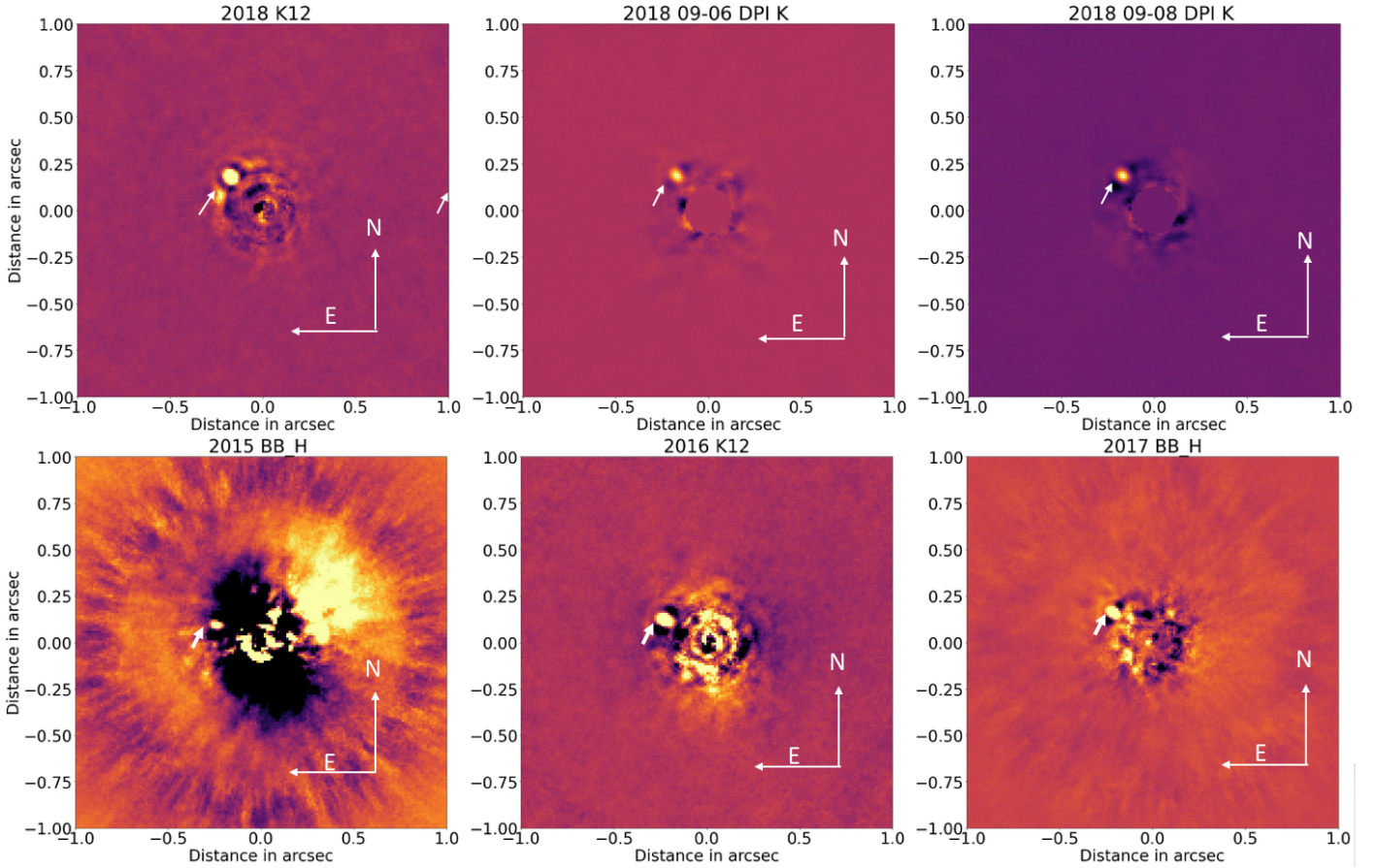
---

[1] https://irdap.readthedocs.io/

Fig. 1. PCA-reduced images showing the detection of HD 206893 B (white arrow). North is up, and east is to the left. The intensity scale is adapted for each epoch according to the intensity peak of the companion.

Table 2. Relative astrometry of HD 206893 B.

MJD	Night	Separation (mas)	PA (°)	Ref
57 299.2	2015-10-03	270.4 ± 2.6	70.0 ± 0.6	[a]
57 647.1	2016-09-15	265.0 ± 2.0	62.3 ± 0.2	[b]
57 948.4	2017-07-13	260.3 ± 2.0	54.0 ± 0.4	[c]
58 289.4	2018-06-19	250.2 ± 3.3	45.5 ± 0.02	[c]
58 367.2	2018-09-05	248.6 ± 4.9	41.8 ± 0.1	[d]
58 369.2	2018-09-07	252.2 ± 3.7	42.5 ± 0.1	[d]

References. [a]Milli et al. (2017). [b]Delorme et al. (2017). [c]Grandjean et al. (2019). [d]This work.

2.3. Astrometry of HD 206893 B

HD 206893 B is clearly detected in all images. Thanks to the sensitivity of SPHERE, it could be monitored from angular separations of 270 mas down to 248 mas during this period. Figure 1 shows images of the companion on the various dates, employing a PCA reduction to remove the starlight. Table 2 provides its relative position in relation to the star, which includes two new astrometric points with respect to Grandjean et al. (2019), obtained using the polarimetric data set reduced in ADI with the ANDROMEDA algorithm (Cantalloube et al. 2015). As these two new points were taken shortly after the previous ones, they do not contribute significantly to further constraining HD 206893 B's orbital parameters (see Figs. B.1 and B.2).

3. Searching for the disk in SPHERE data

3.1. Excluding instrumental effects

Milli et al. (2017) reported a very faint and extended emission along the position angle 60° (east of north) in the data taken on October 3, 2015. However, after visually inspecting the data, we noticed the presence of a mild LWE. This effect is described in Sauvage et al. (2016) and Milli et al. (2018), and it generally degrades the resolution and the accuracy of the target centering behind the coronagraph. In our data set, what we see is a second order effect, making the spider diffraction pattern visible intermittently during the observing sequence (for an illustration of this effect, see Fig. 4 of Milli et al. 2018). Even though this was very tenuous, it did affect a significant percentage of the data. To avoid possible false detections, we discarded all the images from all epochs where the LWE was present. This resulted in 24.5% of the data from the first epoch, in 2015, and 14.4% of the 2017 data being excluded from the analysis.

3.2. Searching for dust emission

The data from all epochs were reduced using cADI with a pixel binning of two. The binning allowed us to increase the sensitivity, and cADI preserves more flux from an extended signal than other reduction techniques such as PCA (Milli et al. 2012). We then computed contrast curves associated with each data set. At this stage we did not correct the contrast curves by the throughput of the algorithm.
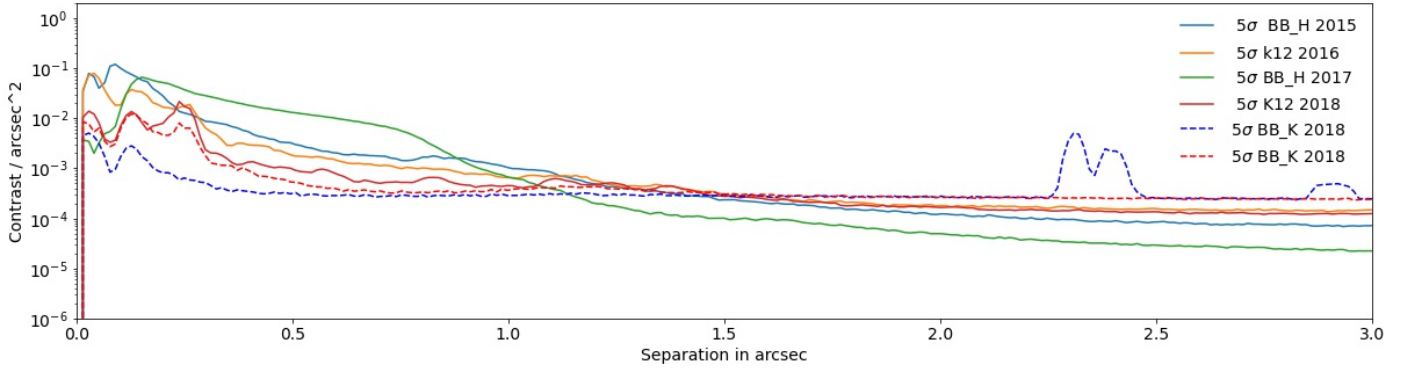
Fig. 2. Five σ contrast expressed per arcsec squared for the four CI-DBI data sets (solid lines), as well as for the DPI data set (dashed lines). Two epochs combined, but we distinguished the polarimetric reduction from the ADI reduction.

Assuming the disk position angle of $61°$ and the inclination of $40°$ suggested by Marino et al. (2020), we tried to separate the region of interest by defining a conical mask oriented along the disk position angle and with an opening angle of $68°$. This should allow the putative disk to be included in the masked area. Separately, we applied the same mask perpendicularly to the disk, isolating an area where one would expect mostly noise (see Fig. A.1).

For each of the mask's orientations, we then computed the azimuthal RMS profile as a function of the separation from the star. When we compared the obtained results, we expected to find greater values in the first case, indicating the presence of a disk.

In Fig. A.2 we provide the azimuthal RMS curves along the two mask orientations for each data set, consisting of the pixel-to-pixel variation along the radial profile from 0 to $6''$. We do not find a significant difference between the results, with the mask positioned along the region of interest showing no signal that is clearly above the noise found in the perpendicular case. We thus conclude that the disk is not detected in scattered light in our SPHERE data sets.

Considering we have different observation periods with different setups (Table 1), we wanted to calculate which data offer the best contrast. For this, we reduced all the data using the same cADI reduction technique. The data obtained in polarimetry have a better sensitivity within one arcsecond than all the other epochs, as shown in Fig. 2.

We then compared two different reduction techniques for the same polarimetric data: PDI, explained in Sect. 2, versus a cADI, where all channels are simply co-added to use the sky-rotation for speckle subtraction. We found the image reduced in ADI to be more sensitive than in PDI beyond $1.3''$, as shown in Fig. 3. An important caveat here is that the noise profile in cADI is not corrected for the self-subtraction inherent to ADI (Milli et al. 2012). A throughput of ~40% was measured with the cADI algorithm at a separation of $3''$ by injecting and retrieving a synthetic disk in the data. This throughput is higher than the typical degree of polarization measured for debris disks at a $90°$ scattering angle (about 20 to 30%; e.g., Arriaga et al. 2020; Ren et al. 2019; Esposito et al. 2018). Therefore, we estimate that the sensitivity of our ADI reduction and, more generally, of our ADI data observations is higher than our polarimetric reduction for this disk.

Finally, we performed the same calculation using reference star differential imaging (RSDI) through a pixel-to-pixel correlation library (Ruane et al. 2017; Xuan et al. 2018). For this we used the data from SHARDDS, with which we built a pixel-by-pixel correlation matrix of all the images that constitute this program.
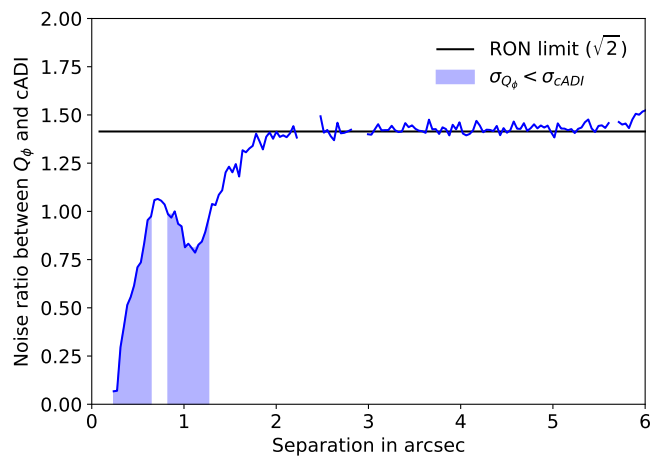

Fig. 3. Ratio between the azimuthal noise profile in the Q_ϕ image and in the cADI-reduced image; both images come from the same observations. The asymptotic value (black line) of $\sqrt{2} = 1.4$ in the readout-noise (RON) limited region comes from the fact that only half the frames are used to obtain the Stokes Q image (respectively Stokes U) when the HWP has a position angle of $0°$ and $45°$ (respectively $22.5°$ and $67.5°$). The sensitivity is higher in the Q_ϕ image compared to the cADI image in the blue-shaded area below $1.28''$.

Given this image library, we were able to build a reference cube with this matrix. As a result, we obtained 775 coronagraphic images of the 24 stars most correlated with those of HD 206893, without including the object of study in the result, to then subtract the halo of the star without generating a self-subtraction as it occurs in cADI. In addition to the above, a synthetic disk was injected into the BB_H 2017 data set, with a maximum surface brightness of 96.0 µJy arcsec^{-2}. This disk can be detected with an ADI reduction (Fig. 4), but it is not detected in reference differential imaging (RDI), hence, RDI is not sensitive enough for such an extended disk. This conclusion is similar to that obtained for point sources by Xuan et al. (2018), who found that ADI processing is more sensitive than RDI processing beyond 0.25 arcseconds.

4. Constraints on the dust albedo

As our study could not confirm the scattered light emission of the disk reported by Milli et al. (2017), we calculated an upper limit on the single-scattering albedo ω using Eq. (2) of Marshall et al. (2018). It assumes a dust absorption opacity
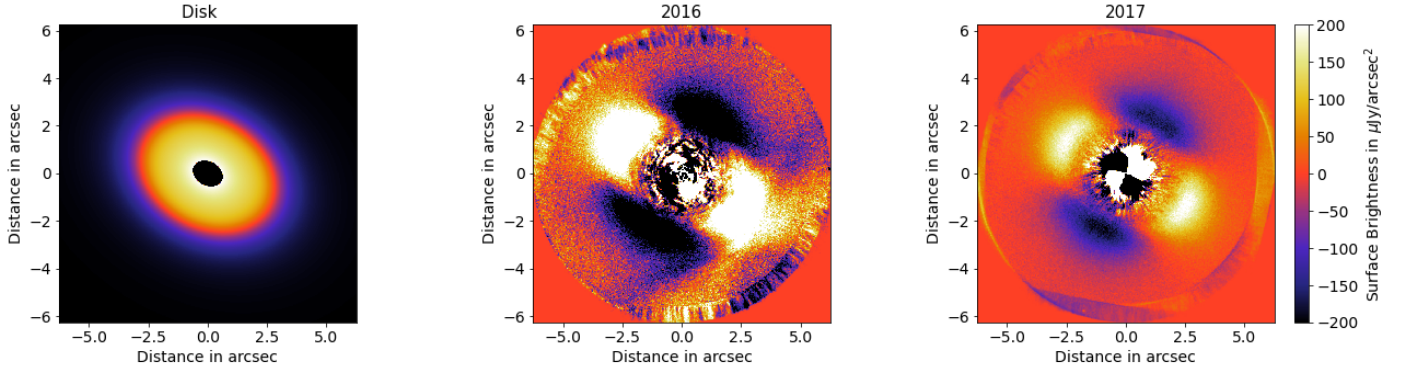
Fig. 4. Simulation of the disk injected in the 2016 and 2017 data sets. The synthetic disk as described by Marino et al. (2020) is shown on the *left*. The images processed with cADI including the injected disk are shown in the *center* and on the *right* for the 2016 and 2017 data sets, respectively. This illustration corresponds to a disk with an albedo equal to 0.9 in the *K* band (2016) and an albedo equal to 0.7 in the *H* band (2017).

Table 3. Upper limits (UL) on the surface brightness and albedo in the *H* and *K* bands for HD 206893.

Night	Filter	Surface brightness UL (mJy arcsec^{-2})	Albedo UL
2016-09-15	*K1-K2*	1.80	0.96
2017-07-13	BB_H	0.096	0.55

constant at optical-to-near-infrared wavelengths and that the scattering is isotropic:

$$\omega = \left(\frac{f * F}{2\pi * \phi * d\phi * S * \cos(i)} + 1 \right)^{-1} , \qquad (1)$$

where S is the surface brightness of the disk in µJy arcsec^{-2}, F is the total star flux in µJy, ϕ is the separation of the scatterers, $d\phi$ is the disk width in arcseconds, i is the inclination, and f is the fractional luminosity.

The minimum albedo enabling the detection of the disk was calculated through an iterative process in which a synthetic disk was created, as shown in Fig. 4. This disk was injected into the corresponding data sets of different epochs at 1.6 and 2.2 microns, respectively, assuming the disk morphology presented by Marino et al. (2020), with the exception of the gap at 74 au: a position angle of 61°, an inclination of 40°, and an extension from 30 to 180 au.

The disk is no longer detectable when the surface brightness is below the values shown in Table 3 in the *H* and *K* bands, allowing us to establish an upper limit on the disk's albedo. Given the small uncertainty on the disk inclination, ±3° (Marino et al. 2020), the maximum albedo is well constrained as it is nearly constant for that small range of inclinations.

These upper limits can marginally constrain the composition or minimum grain size of the dust population in the system. From the analysis presented in Choquet et al. (2018, Fig. 11, bottom), a composition of pure water ice can already be excluded if the population is dominated by particles smaller than a few tens of microns. Interestingly, we note that one debris disk with a similar inclination and surrounding another F5V star is known to possess an albedo as high as 0.6 in the near-infrared: HD 181327 (Schneider et al. 2006), located between 50 and 125 au. In this case, independent analysis based on the SED suggested that the dust particles are icy, with a volume fraction of water ice as

high as 67% (Lebreton et al. 2012). We can, therefore, exclude a dust composition similar to that of HD 181327. A significant difference between HD 206893 and HD 181327 is the age of the system: HD 181327 is a much younger system, part of the β Pic moving group, with an estimated age of $18.5^{+2.0}_{-2.4}$ Myr (Miret-Roig et al. 2020). CO emission is detected around HD 181327, with a mass ranging between $1.2 \times 10^{-6} M_\oplus$ and $2.9 \times 10^{-6} M_\oplus$ (Marino et al. 2016), whereas only an upper limit on the CO $J = 2-1$ transition regarding HD 206893 was estimated: $2.4 \times 10^{-6} M_\oplus$ (Marino et al. 2020).

The future Near Infrared Camera instrument (NIRCam) on board the *James Webb* Space Telescope (JWST) will offer an improved sensitivity that will allow us to attempt to detect the scattered light of the disk. The JWST exposure time calculator (ETC) predicts a 3σ sensitivity of 60µJy arcsec^{-2} for a 1h on-source exposure time, in the background-limited regime, using the F200W filter and the MASK210R coronagraph. This provides a 40% improvement compared to what was achieved with SPHERE in the *H* band in 2.7 h of on-source exposure time and opens up the perspective of detecting the disk in scattered light if the single-scattering albedo at 2 µm is larger than 0.5.
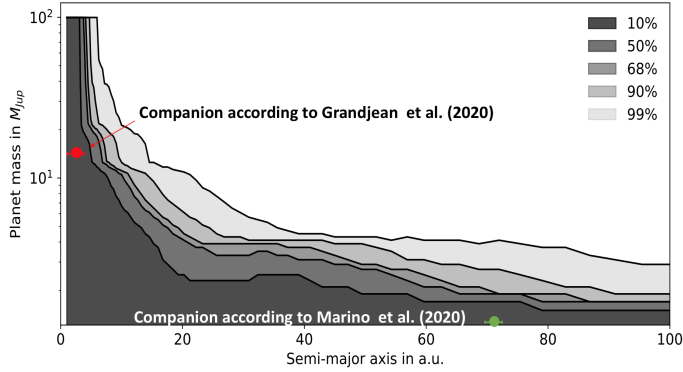
5. Probability of detecting additional companions

Considering the data described in Sect. 2, we used the Multi-epoch multi-purpose Exoplanet Simulation System (MESS2; Lannier et al. 2017), a Monte-Carlo based algorithm, to compute the probability of detecting a companion through direct imaging as a function of its mass and its semimajor axis.

For this purpose, we first created 2D maps of our detection limits using the ANDROMEDA algorithm that yields the best detection limits. We used only the four data sets obtained in the CI or DBI epochs because the polarimetric data were obtained within less than three months of the previous epoch and have less field rotation. These contrast detection limits are then expressed in Jupiter masses, assuming an age of 200 Myr for the system and using the AMES-Cond model (Allard et al. 2001). MESS2 then generates random Keplerian orbits for companions in a mass versus semimajor axis grid and tests whether they are recovered based on the detection limit maps to retrieve the probability of detection for each grid point. The mesh of the grid is detailed in Table 4, along with the range of eccentricities and inclinations explored by the 5000 randomly selected orbits for each grid point with a flat distribution. The results are shown in Fig. 5. As expected, the companion detection capability improves with

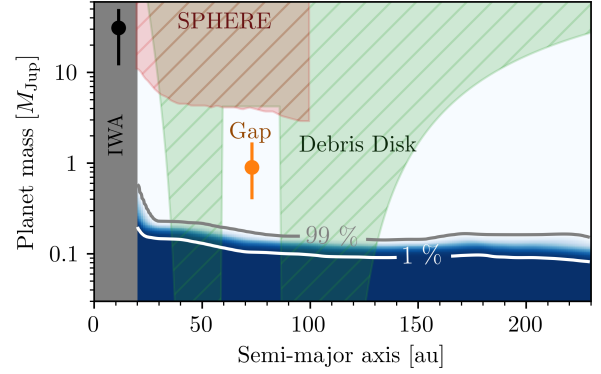**Table 4.** Boundaries for the orbital parameters generated by MESS2.

Variable	Min	Max	Number of steps
Semimajor axis (au)	1	100	100
Mass (M_{Jup})	0.1	100	100
Eccentricity	0	0.6	–
Inclination (deg)	25	40	–

Fig. 5. Probability map of detecting a companion around HD 206893 as a function of its mass and semimajor axis, assuming an age of 200 Myr. The position of the RV candidate proposed by Grandjean et al. (2019) is indicated in red. The position of the putative companion proposed by Marino et al. (2020) is indicated in green.

Fig. 6. JWST MIRI 15 µm detection probability as a function of planet mass and semimajor axis for a 1h integration, taking into account the system's inclination, age uncertainty, and probability of reaching a 5σ level. The contours show the 99 and 1% probabilities. The orange error bar shows the predicted planet carving the gap. The red and green hatched regions are excluded since no planets were detected with SPHERE (red) and a planet in that region would disrupt the disk or push their edges away from where they are observed with ALMA (green). The gray region represents the inner working angle (IWA) of JWST in this mode.

increasing distance from the star. The detection probability is 90% for masses of 2.5 M_{Jup} at 74 au and masses above 55 M_{Jup} between 1.4 and 2.6 au.

As estimated by Marino et al. (2020), the disk extends from 30 to 180 au, with a maximum brightness at 120 au, surface density peak at 114^{+5}_{-7} au, and a 27 ± 5 au wide gap at 74 ± 3 au, which could be caused by a planet of $0.9^{+0.8}_{-0.5}$ M_{Jup}. The probability of detecting the putative planet is below 10% according to our model. We thus conclude that we do not have the sensitivity with the present data to detect a sub-Jovian planet, such as the Marino et al. (2020) presumed companion.

Despite SPHERE's limitation, JWST should be able to detect a sub-Jovian planet with its expected high sensitivity at thermal IR. To quantify this, we simulated a 1 h integration with the JWST Mid-Infrared Instrument (MIRI) 15 µm coronagraphy mode using PANCAKE[2] (Van Gorkom et al. 2016; Schneider et al. 2016; Perrin et al. 2018; Girard et al. 2018; Carter et al. 2020), which is based on the official JWST ETC Pandeia (Pontoppidan et al. 2016). We then extracted a contrast curve from this simulated observation, which we then used to produce a planet mass versus semimajor axis detectability map, as shown in Fig. 6. This map was produced as follows. Each planet mass was translated to a magnitude contrast using Bern EXoplanet models (BEX; Linder et al. 2019), the latest models for 0.02–2 M_{Jup} planets formed through core accretion, and assuming an age of 200 Myr. Then, at each point in this map, we produced an ensemble of random points with different separations along the orbit of the planet. We assumed a circular orbit that is inclined in line with the debris disk and determined the likelihood of it leading to a 5σ detection. Then, the probability in this detectability map is the likelihood of a planet of that mass and semimajor

axis reaching a $>5\sigma$ detection. We note that we do not expect these planets to have eccentricities greater than $\gtrsim 0.1$ based on the already observed levels of axisymmetry in this disk.

Figure 6 shows that the putative planet at the gap (orange error bar) would be easily detected with a 1 h integration. The red and green regions are excluded by the SPHERE observations presented here and by ALMA observations that imaged the disk, respectively. The white region represents planet masses and semimajor axes that would be detected by JWST observations. This demonstrates the discovery potential of JWST, which will allow these types of putative planets to be confirmed or ruled out. Moreover, such observations could also reveal the presence of a planet sculpting the disk's inner edge near 30 au, with a mass between 0.2 and 5 M_{Jup}, which could have been missed by our SPHERE observations.

Finally, as the Grandjean et al. (2019) RV companion is angularly very close to the star (typically less than 70 mas), we see from Fig. 5 that a detection in direct imaging with SPHERE is not possible. Nevertheless, *Gaia* will allow its characterization.

6. Concluding remarks and perspectives

We analyzed six SPHERE data sets of HD 206893 obtained between 2015 and 2018. HD 206893 B is detected in all six data sets, from a separation of 267 mas in 2015–50 mas in 2018. These values comply with what was reported by Grandjean et al. (2019). In addition, we obtained two new astrometric points using the polarimetry data, with separations of 248.5 and 252.2 mas. Nevertheless, due to their proximity in time with previous points, these did not further constrain the companion's orbital parameters.

Using every image available, we establish upper limits to the detection of possible additional planets in the disk: 90% for masses above 55 M_{Jup} between 1.4 and 2.6 au and masses of 2.5 M_{Jup} at 74 au. Consequently, the planets inferred from RV data and from the disk gap detected in ALMA images are not detectable with these six SPHERE epochs.

Reducing all of our data with the cADI technique has shown that the polarimetry data have the best sensitivity within one

---

[2] https://github.com/spacetelescope/pandeia-coronagraphy

arcsecond. Given the throughput of ~40% at 3″ obtained by injecting and retrieving a synthetic disk in the data, we estimate that our ADI reduction has a greater sensitivity than PDI for this particular disk. Even though we excluded data that could lead to false detections and applied different techniques to increase the sensitivity, we do not detect the scattered light of the debris disk in the present data set.

From the surface brightness upper limits that we derived assuming the morphology presented by Marino et al. (2020), we can conclude that the single-scattering albedo of the disk is <0.55 in the H band and <0.96 in the K band. Based on these upper limits, we can rule out a disk composition of pure water ice if the dust is dominated by particles smaller than a few tens of microns, but stronger constraints on the size or composition cannot be made.

Despite these results, the possibility of successfully resolving the debris disk using another technique should not be excluded. One possible approach is to use RSDI, either from a machine-learning-based library, currently under study by C. Romero et al. (in prep.), or a second star close to the target during the same observation night (hopping). Moreover, assuming the single-scattering albedo at 2 μm to be larger than 0.5, the future JWST instrument NIRCam might offer the possibility of detecting the disk in scattered light thanks to its increased sensitivity.

References

Allard, F., Hauschildt, P., Alexander, D., Tamanai, A., & Schweitzer, A. 2001, ApJ, 556, 357
Arriaga, P., Fitzgerald, M. P., Duchêne, G., et al. 2020, AJ, 160, 79
Beuzit, J.-L., Vigan, A., Mouillet, D., et al. 2019, A&A, 631, A155
Cantalloube, F., Mouillet, D., Mugnier, L. M., et al. 2015, A&A, 582, A89
Cantalloube, F., Por, E. H., Dohlen, K., et al. 2018, A&A, 620, L10
Cantalloube, F., Farley, O. J. D., Milli, J., et al. 2020, A&A, 638, A98
Carbillet, M., Bendjoya, P., Abe, L., et al. 2011, Exp. Astron., 30, 39
Carter, A. L., Hinkley, S., Bonavita, M., et al. 2020, MNRAS, 501, 1999
Chen, C. H., Mittal, T., Kuchner, M., et al. 2014, ApJS, 211, 25
Choquet, É., Bryden, G., Perrin, M. D., et al. 2018, ApJ, 854, 53
de Boer, J., Langlois, M., van Holstein, R. G., et al. 2020, A&A, 633, A63
Delorme, P., Schmidt, T., Bonnefoy, M., et al. 2017, A&A, 608, A25
Dohlen, K., Langlois, M., Saisse, M., et al. 2008, Proc. SPIE, 7014, 851
Esposito, T. M., Duchêne, G., Kalas, P., et al. 2018, AJ, 156, 47
Esposito, T. M., Kalas, P., Fitzgerald, M. P., et al. 2020, AJ, 160, 24
Gaia Collaboration (Brown, A. G. A., et al.) 2018, A&A, 616, A22
Girard, S., Allanche, T., Paillet, P., et al. 2018, IEEE Transac. Nucl. Sci., 65, 1612
Grandjean, A., Lagrange, A.-M., Beust, H., et al. 2019, A&A, 627, A22
Guerri, G., Daban, J.-B., Robbe-Dubois, S., et al. 2011, Exp. Astron., 30, 59
Høg, E., Fabricius, C., Makarov, V. V., et al. 2000, A&A, 355, L27
Hughes, A. M., Duchêne, G., & Matthews, B. C. 2018, ARA&A, 56, 541
Langlois, M., Dohlen, K., Vigan, A., et al. 2014, Proc. SPIE, 9147, 657
Lannier, J., Lagrange, A. M., Bonavita, M., et al. 2017, A&A, 603, A54
Lebreton, J., Augereau, J. C., Thi, W. F., et al. 2012, A&A, 539, A17
Linder, E. F., Mordasini, C., Mollière, P., et al. 2019, A&A, 623, A85
Marino, S., Matrà, L., Stark, C., et al. 2016, MNRAS, 460, 2933
Marino, S., Zurlo, A., Faramaz, V., et al. 2020, MNRAS, 498, 1319
Marois, C., Lafrenière, D., Doyon, R., Macintosh, B., & Nadeau, D. 2006, ApJ, 641, 556
Marshall, J. P., Milli, J., Choquet, É., et al. 2018, ApJ, 869, 12
Milli, J., Mouillet, D., Lagrange, A.-M., et al. 2012, A&A, 545, A111
Milli, J., Hibon, P., Christiaens, V., et al. 2017, A&A, 597, L2
Milli, J., Kasper, M., Bourget, P., et al. 2018, Proc. SPIE, 10703, 752
Miret-Roig, N., Galli, P. A. B., Brandner, W., et al. 2020, A&A, 642, A179
Moór, A., Ábrahám, P., Derekas, A., et al. 2006, ApJ, 644, 525
Nederlander, A., Hughes, A. M., Fehr, A. J., et al. 2021, ApJ, submitted [arXiv:2101.08849]
Perrin, M. D., Pueyo, L., Van Gorkom, K., et al. 2018, Proc. SPIE, 10698, 1069809
Pontoppidan, K. M., Pickering, T. E., Laidler, V. G., et al. 2016, Proc. SPIE, 9910, 991016
Ren, B., Choquet, É., Perrin, M. D., et al. 2019, ApJ, 882, 64
Ruane, G., Mawet, D., Kastner, J., et al. 2017, AJ, 154, 73
Sauvage, J.-F., Fusco, T., Lamb, M., et al. 2016, Proc. SPIE, 9909, 990916
Schneider, G., Silverstone, M. D., Hines, D. C., et al. 2006, ApJ, 650, 414
Schneider, G., Grady, C. A., Stark, C. C., et al. 2016, AJ, 152, 21
Soummer, R., Pueyo, L., & Larkin, J. 2012, ApJ, 755, L28
Van Gorkom, K., Pueyo, L., Lajoie, C.-P., & JWST Coronagraphs Working Group. 2016, AAS Meeting Abstracts, 228, 317.03
van Holstein, R. G., Snik, F., Girard, J. H., et al. 2017, Proc. SPIE, 10400, 315
van Holstein, R. G., Girard, J. H., de Boer, J., et al. 2020, A&A, 633, A64
Vigan, A., Moutou, C., Langlois, M., et al. 2010, Proc. SPIE, 7735, 1162
Vigan, A., Fontanive, C., Meyer, M., et al. 2021, A&A, in press, https://doi.org/10.1051/0004-6361/202038107
Wahhaj, Z., Milli, J., Kennedy, G., et al. 2016, A&A, 596, L4
Xuan, W. J., Mawet, D., Ngo, H., et al. 2018, AJ, 156, 156
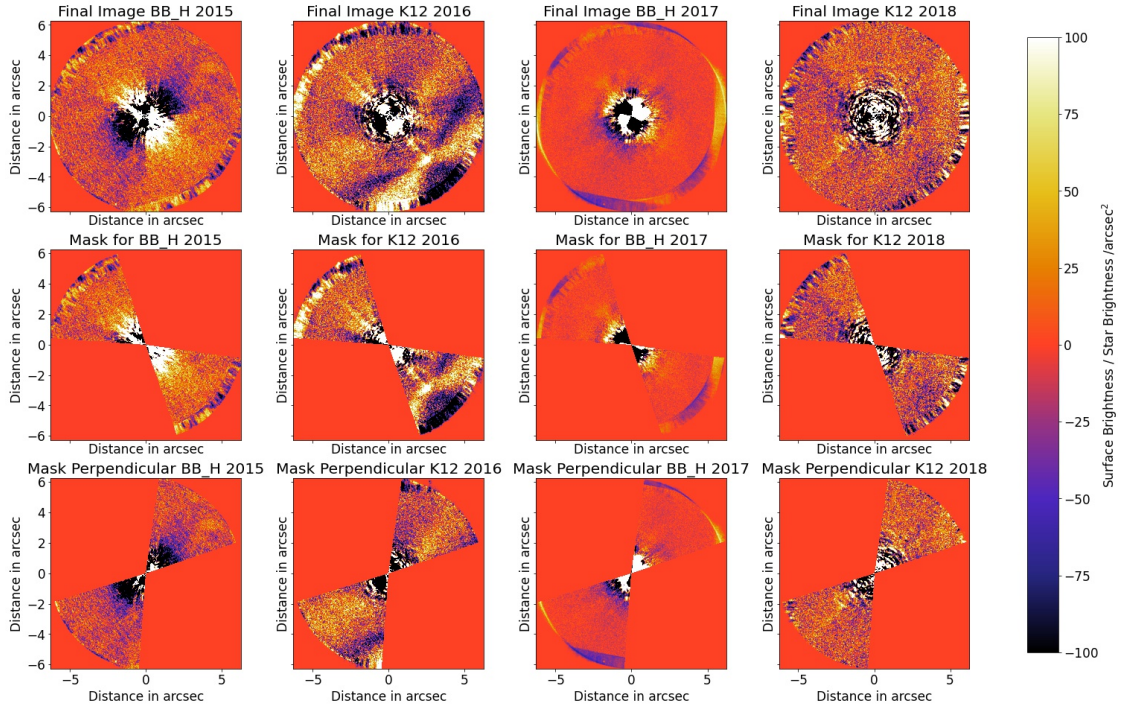
Appendix A: Masking the disk

Fig. A.1. Reduced images (*top row*), mask created to segment the area of interest where the disk would be (*middle row*), and its perpendicular to make the comparison between them (*bottom row*).
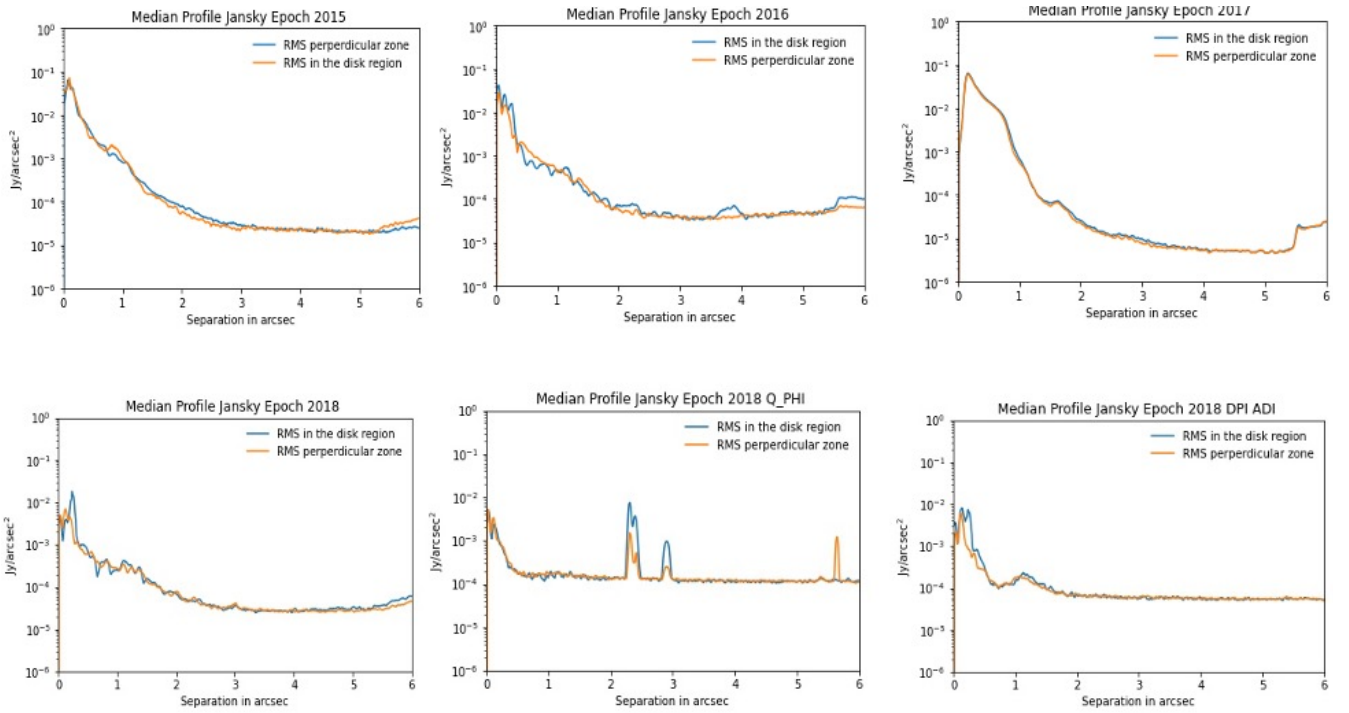

Fig. A.2. Radial curves of the noise in the corresponding area of interest (solid blue line) versus the same profile but at 90° where no signal is expected (solid orange line).
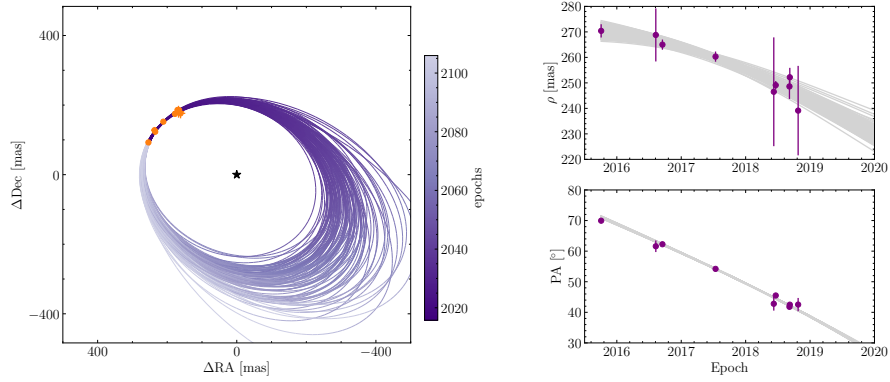
Appendix B: Orbital constraints

Fig. B.1. Possible orbits for HD 206893 B (*left*) using the same methodology as Marino et al. (2020) and adding the astrometric points from the polarimetric data. The data points are shown in orange, and the respective separations and parallactic angles are shown on the *right*.
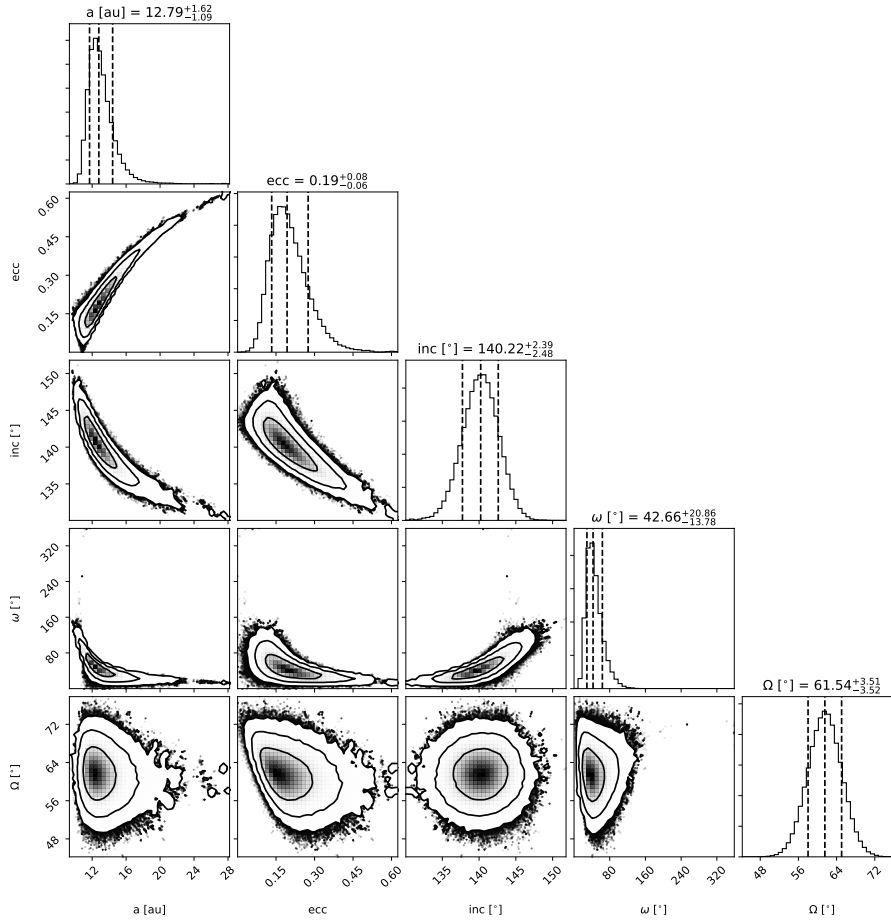

Fig. B.2. Posterior distribution of the semimajor axis, eccentricity, inclination, argument of pericenter, and longitude of ascending node. The vertical dashed lines represent the 16th, 50th, and 84th percentiles, and the contours the 68, 95, and 99.7% confidence regions. This plot was generated following the same procedure used by Marino et al. (2020).